The Astrophysical Journal, 948:121 (12pp), 2023 May 10 https://doi.org/10.3847/1538-4357/acbc1b

Understanding the Relationship between Solar Coronal Abundances and F10.7 cm Radio Emission

Andy S. H. To[1], Alexander W. James[1,2], T. S. Bastian[3], Lidia van Driel-Gesztelyi[1,4,5], David M. Long[1,6], Deborah Baker[1], David H. Brooks[7], Samantha Lomuscio[3], David Stansby[1], and Gherardo Valori[8]
[1] University College London, Mullard Space Science Laboratory, Holmbury St. Mary, Dorking, Surrey, RH5 6NT, UK; shu.to.18@ucl.ac.uk
[2] European Space Agency (ESA), European Space Astronomy Centre (ESAC), Camino Bajo del Castillo, s/n, E-28692 Villanueva de la Cañada, Madrid, Spain
[3] National Radio Astronomy Observatory (NRAO), 520 Edgemont Road, Charlottesville, VA 22903, USA
[4] LESIA, Observatoire de Paris, Université PSL, CNRS, Sorbonne Université, Univ. Paris Diderot, Sorbonne Paris Cité, 5 place Jules Janssen, F-92195 Meudon, France
[5] Konkoly Observatory, Research Centre for Astronomy and Earth Sciences, Hungarian Academy of Sciences, Konkoly Thege út 15-17., H-1121, Budapest, Hungary
[6] Astrophysics Research Centre, School of Mathematics and Physics, Queen's University Belfast, University Road, Belfast, BT7 1NN, Northern Ireland, UK
[7] College of Science, George Mason University, 4400 University Drive, Fairfax, VA 22030, USA
[8] Max-Planck-Institut für Sonnensystemforschung, Göttingen, Germany
Received 2022 August 31; revised 2023 February 8; accepted 2023 February 13; published 2023 May 15

Abstract

Sun-as-a-star coronal plasma composition, derived from full-Sun spectra, and the F10.7 radio flux (2.8 GHz) have been shown to be highly correlated ($r = 0.88$) during solar cycle 24. However, this correlation becomes nonlinear during increased solar magnetic activity. Here we use cotemporal, high spatial resolution, multiwavelength images of the Sun to investigate the underlying causes of the nonlinearity between coronal composition (FIP bias) and F10.7 solar index correlation. Using the Karl G. Jansky Very Large Array, Hinode/EIS (EUV Imaging Spectrometer), and the Solar Dynamics Observatory, we observed a small active region, AR 12759, throughout the solar atmosphere from the photosphere to the corona. The results of this study show that the magnetic field strength (flux density) in active regions plays an important role in the variability of coronal abundances, and it is likely the main contributing factor to this nonlinearity during increased solar activity. Coronal abundances above cool sunspots are lower than in dispersed magnetic plage regions. Strong magnetic concentrations are associated with stronger F10.7 cm gyroresonance emission. Considering that as the solar cycle moves from minimum to maximum, the sizes of sunspots and their field strength increase with the gyroresonance component, the distinctly different tendencies of radio emission and coronal abundances in the vicinity of sunspots is the likely cause of saturation of Sun-as-a-star coronal abundances during solar maximum, while the F10.7 index remains well correlated with the sunspot number and other magnetic field proxies.

Unified Astronomy Thesaurus concepts: Solar corona (1483); Solar magnetic fields (1503); Solar radio emission (1522); Solar abundances (1474)

1. Introduction

The F10.7 cm radio flux index is one of the most widely used solar indices to characterize solar activity. Daily measurements of the Sun-as-a-star F10.7 cm flux stretch back to 1947. Cycle-to-cycle F10.7 cm observations show that the maximum flux could vary by a factor of 2–3 (Floyd et al. 2005; Tapping 2013). On the other hand, recent observations of the solar wind have also shown a cyclic behavior of elemental abundances (Kasper et al. 2007; McIntosh et al. 2011; Lepri et al. 2013). Brooks et al. (2017) observed a correlation between solar coronal abundances and the F10.7 cm radio flux, implying that coronal abundances change with the solar cycle phase. This, in turn, suggests that coronal abundances are influenced by magnetic activity and the coronal heating process, with significant implications for solar-like stars as well. These stars may also show cyclic effects, and the chemical composition of their coronae likely depends on magnetic activity rather than just the fixed properties of the star. However, a saturation of the first ionization potential (FIP) bias is often observed in high-activity stars (Wood & Linsky 2010; Laming 2015; Seli et al. 2022), with a typical FIP bias of ∼1 or lower. In fact, this saturation is also observed in Brooks et al. (2017). During high to extreme solar activity, the correlation between F10.7 and FIP bias becomes nonlinear; Sun-as-a-star FIP bias appears to be saturated, while F10.7 cm flux continues to go up with the solar activity. The reason behind the FIP bias saturation of both the Sun and highly active stars remains poorly understood. Investigating and understanding the root cause of the F10.7–FIP bias nonlinearity and being able to account for it provide invaluable insight into the solar activity, stellar magnetic fields, and both solar and stellar coronal heating.

The first step to quantify the nonlinearity is to understand elemental abundance variations. Elemental abundances have long been used as an indicator for the physical processes throughout astrophysics. The benchmark reference for all cosmic applications is the solar chemical composition. Understanding the spatial and temporal variations in the composition of the solar corona provides insight into different physical processes of the Sun, including reconnections in the corona, how matter and energy flow from the chromosphere, where the plasma is separated according to chemical populations (i.e., fractionated), and how (fractionated) plasma flows out into the heliosphere. The method to study and quantify solar and stellar elemental fractionation is to use the FIP of elements in the solar atmosphere. High-FIP elements (i.e., FIP $>$ 10 eV) maintain

their photospheric abundances in the corona, whereas low-FIP elements can have enhanced abundances up to a factor of 4^{+} (i.e., FIP bias). This is the well-known FIP effect. Conversely, the inverse FIP effect refers to the relative enhancement of high-FIP or relative depletion of low-FIP elements in solar and stellar coronae.

The level of enhancement of the low-FIP elements in the Sun's atmosphere is far from uniform. The FIP bias values depend on factors such as an active region's age, evolutionary stage, and the surroundings of active region. In open-field coronal holes, FIP bias remains unaltered, maintaining a photospheric value of around 1 (Feldman et al. 1998; Brooks & Warren 2011; Baker et al. 2013). Quiet-Sun regions typically have a FIP bias in the range of 1.5–2 (Warren 1999; Baker et al. 2013; Ko et al. 2016), with the highest FIP bias of 3–4 observed in specific locations in solar active regions (Baker et al. 2013, 2015, 2018, 2021; Del Zanna & Mason 2014; To et al. 2021; Mihailescu et al. 2022). When an active region begins emerging, it is still dominated by photospheric plasma, and it takes hours to days for the coronal loops to reach peak elemental fractionation values. As the active region begins to decay, the FIP bias slowly returns to that of the surrounding coronal structure (Ko et al. 2016; Baker et al. 2018).

The temporal variation of composition could also extend beyond hours and days to solar cycle timescales of many years. This was indeed shown by Brooks et al. (2017), who used data from the EUV Variability Experiment (Woods et al. 2012) on the Solar Dynamics Observatory (SDO; Pesnell et al. 2012) to determine daily Sun-as-a-star FIP bias values from solar minimum to solar maximum during cycle 24. It was demonstrated that the FIP bias derived from full-Sun spectra is highly correlated ($r = 0.88$) with the F10.7 cm radio flux, a solar activity proxy, during a 4 yr interval (2010–2014; Brooks et al. 2017, Supplementary Figure 2). However, the relationship between coronal elemental composition and the F10.7 cm radio flux appears to become nonlinear for the periods of mid-2011/early 2012 and mid-2013/early 2014, when the Sun approached its maximum activity. The FIP bias did not grow in tandem with the F10.7 radio flux but instead appeared to saturate.

The second step to understand this nonlinearity is to examine the emission mechanisms of the F10.7 cm radio flux. Similar to FIP bias values, F10.7 cm emission varies spatially, depending on different solar structures. There are two contributions to the observed radio emission: thermal bremsstrahlung and gyroresonance emission. Various studies have considered the source of these two emission components, with similar suggestions that the bremsstrahlung emission originates from the plage regions (Felli et al. 1981; Tapping & Detracey 1990; Tapping et al. 2003), while suggesting that gyroresonance emission comes from the strong magnetic fields in active regions (Schmahl & Kundu 1995, 1998; de Wit et al. 2014; Schonfeld et al. 2015). Henney et al. (2012) analyzed the correlation between the photospheric magnetic field and the F10.7 flux. They characterized magnetic "plage" regions as areas with local field strengths of 25–150 G and the active region component as originating from a field with a strength >150 G and could predict the bremsstrahlung component of the F10.7 cm emission well, which also correlates well with the solar extreme-ultraviolet (EUV) flux (White et al. 2000, Schonfeld et al. 2015, 2017, 2019). However, spatially resolved maps linking F10.7 radio flux to coronal composition have never been investigated. In this paper, we present Hinode/EUV Imaging Spectrometer (EIS) observations of AR 12759 taken on 2020 April 3 and 7 to investigate the contribution of the F10.7 radio flux (2.8 GHz) to elemental fractionation. As previously noted, the correlation between F10.7 flux and coronal abundances has been observed to change under different solar activity conditions (Brooks et al. 2017). For the first time, these EIS observations are compared with the SDO EUV magnetic field data and the spatially resolved Stokes I and V maps of the F10.7 flux observed by the Karl G. Jansky Very Large Array (JVLA; Perley et al. 2011). The observations are presented in Section 2, with results and discussion in Sections 3 and 4, respectively. Conclusions are then presented in Section 5.

2. Observations and Data Analysis

The small and simple bipolar active region AR 12759 was visible on the northern hemisphere of the Sun from 2020 March 30 to April 10, as shown in the Atmospheric Imaging Assembly (AIA; Lemen et al. 2012) 193 Å and Helioseismic and Magnetic Imager (HMI; Scherrer et al. 2012) magnetogram of Figure 1. The active region was in its early decay phase when it rotated onto the disk, with a positive-polarity leading spot containing a light bridge, and pore-like transient spots in the following (negative-polarity) region were present until April 4. An ephemeral region emerged in the active region's trailing part from about 21:00 UT on the 3rd, forming pores, which also disappeared on the 4th. No more spots were seen in the active region after that. Two sets of observations were obtained on 2020 April 3 and 7 during a joint observation campaign by the JVLA and Hinode/EIS.

2.1. Coronal EUV Observation and Alignment

Details of the two EIS observations made at 13:42 UT on 2020 April 3 and 16:01 UT on 2020 April 7 can be found in Table 1. In this study, we use the Si X 258.38 Å/S X 264.23 Å intensity ratio to examine the spatially averaged changes in the coronal (~1.25–1.5 MK) FIP bias in a few locations (blue, orange, black, and red contours of Figure 1). To minimize effects caused by temperature and density variations, 16 consecutive Fe lines from Fe VIII to Fe XVI were used in the calculation of the differential emission measure (DEM). We used the Markov Chain Monte Carlo (MCMC) algorithm distributed with the PINTofALE spectroscopy package (Kashyap & Drake 1998, 2000) and contribution functions taken from the CHIANTI Atomic Database, Version 9.0 (Dere et al. 1997, 2019). We also used the photospheric abundances of Grevesse et al. (2007), assuming the density calculated through the fitted Fe XIII 202.04 Å/203.83 Å intensity ratio. As both Fe and Si are low-FIP elements, we scaled the emission measure to reproduce the observed intensity of Si X 258.38 Å. The Si/S FIP bias is then the ratio of the predicted to observed intensity of the S X 264.23 Å emission line. A more detailed description of the procedures to calculate a coronal composition map can be found in Brooks & Warren (2011). This method minimizes the effects of temperature and density when compared to only taking the Si/S intensity ratio.

One source of error is misalignment of the different instruments. As our results compare observations from Hinode/EIS, JVLA, and SDO/AIA that are formed at drastically different solar altitudes, several steps were taken

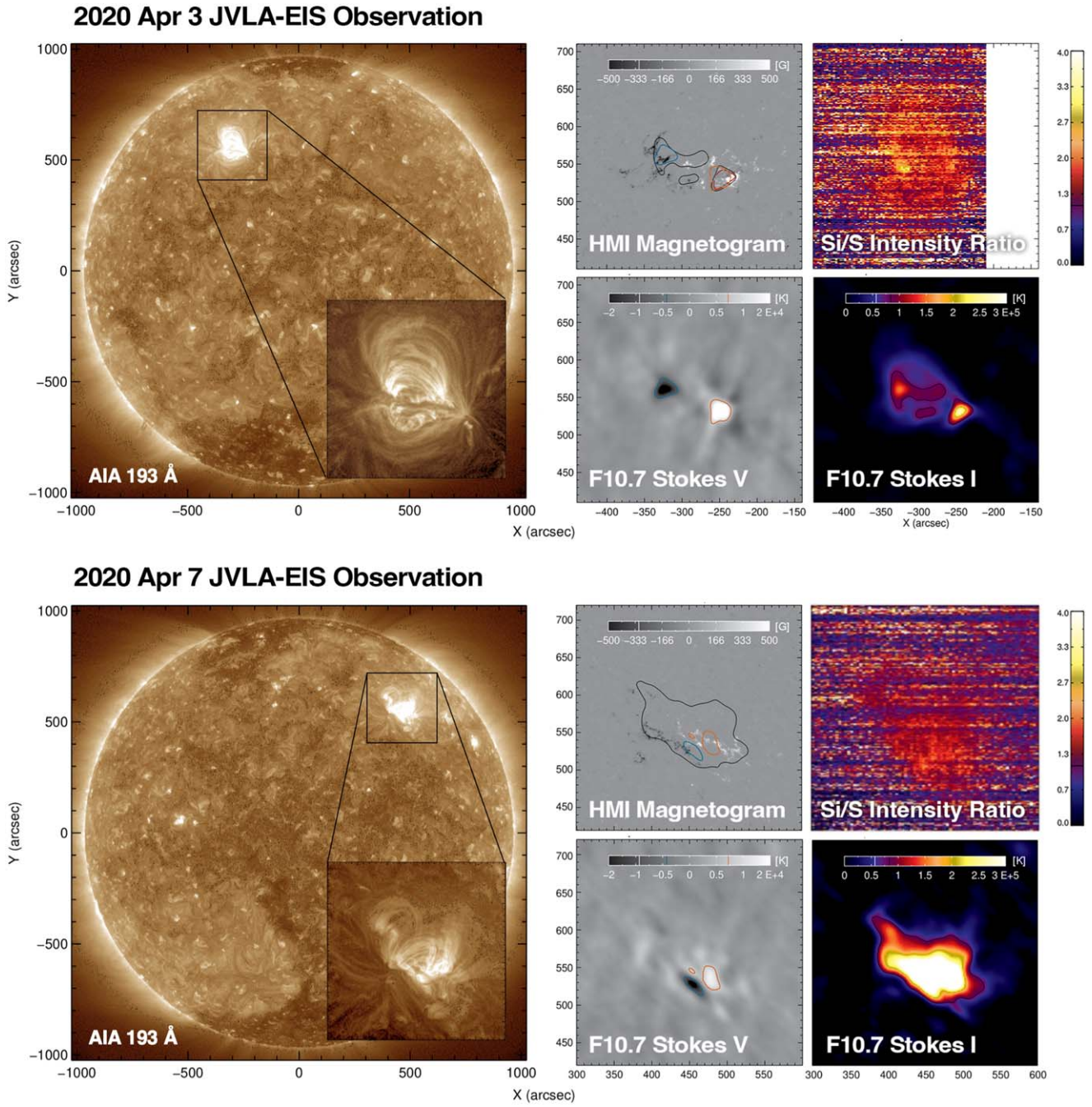

Figure 1. Small bipolar active region AR 12759, observed during the JVLA/20A-047 observing campaign on April 3 and 7. Left to right, top to bottom: AIA 193 Å, HMI magnetogram, Si X 258.38 Å/S X 264.23 Å intensity ratio map, F10.7 radio flux map (Stokes V), and F10.7 radio flux map (Stokes I). Four F10.7 cm regions are used in this paper to calculate the FIP bias: (1) a Stokes I region with a brightness temperature >80,000 K subtracted by strong Stokes V emission (black contour), (2) negative Stokes V regions with a brightness temperature <−10,000 K (blue contour), (3) a positive Stokes V region with brightness temperature >10,000 K (orange contour), and (4) the estimated gyroresonance region on April 3 defined using ((Stokes I-modeled free–free)/Stokes I) (red dashed contour; Section 4.1). It can be seen that the negative Stokes V region is associated with the following polarity, whereas the positive Stokes V and gyroresonance regions are associated with the leading polarity. The Si/S intensity ratio maps shown here are for demonstration purposes. In our analysis, we calculated and used the spatially averaged FIP bias. This significantly improves the signal-to-noise ratio.

to minimize the instrumental offset between the three instruments. First, the AIA coordinate system was used as our base coordinate system. Second, as the active region was stable throughout the EIS raster duration, the Fe XII 195.12 Å intensity maps observed by EIS were aligned with an AIA 193 Å image taken at the beginning raster time. Lastly, to align JVLA to EIS and AIA, we followed the approach of White et al. (2000) and Schonfeld et al. (2015) to estimate the free–free component of the F10.7 flux using AIA DEM (Hannah & Kontar 2012). This allowed us to visualize F10.7 flux data in AIA coordinates. The F10.7 cm bremsstrahlung emission taken by JVLA was then aligned to this predicted emission. As a final check, the coronal magnetic field of AR 12759 was modeled by extrapolating radial field magnetograms that were taken by HMI on April 3 and 7 (see Section 2.3). The F10.7 cm gyroresonance observations at 2.8 GHz originate from thin

Table 1
Hinode/EIS Study Details Used in This Work

Study number	569
Raster acronym	HPW021VEL260x512v2
Emission lines	Fe VIII 185.213 Å, Fe VIII 186.601 Å Fe IX 188.497 Å, Fe IX 197.862 Å Fe X 184.536 Å, Fe XI 188.216 Å Fe XII 192.394 Å, Fe XII 195.119 Å Fe XIII 202.044 Å, Fe XIII 203.826 Å Fe XIV 264.787 Å, Fe XIV 270.519 Å Fe XV 284.16 Å, Fe XVI 262.984 Å Fe XVII 254.870 Å Si X 258.38 Å, S X 264.23 Å Ca XIV 193.87 Å, Ar XIV 194.40 Å
Field of view	260″ × 512″
Rastering	2″ slit, 87 positions, 3″ coarse steps
Exposure time	60 s
Total raster time	1 hr
Reference spectral window	Fe XII 195.12 Å
Study number	544
Raster acronym	AbundRaster_v3
Emission lines	Fe VIII 185.213 Å, Fe VIII 186.601 Å Fe IX 188.497 Å, Fe IX 197.862 Å Fe X 184.536 Å, Fe XI 188.216 Å Fe XII 192.394 Å, Fe XII 195.119 Å Fe XIII 202.044 Å, Fe XIII 203.826 Å Fe XIV 264.787 Å, Fe XIV 270.519 Å Fe XV 284.16 Å, Fe XVI 262.984 Å Si X 258.38 Å, S X 264.23 Å Ca XIV 193.87 Å, Ar XIV 194.40 Å
Field of view	492″ × 512″
Rastering	2″ slit, 123 positions, 4″ coarse steps
Exposure time	30 s
Total raster time	3 hr
Reference spectral window	Fe XII 195.12 Å

isogauss layers with constant magnetic field strengths of $B = 500$ (second harmonic) and 333 G (third harmonic; White & Kundu 1997). To investigate the sources of F10.7 cm emission, we modeled the coronal magnetic field of AR 12759 using a linear force-free field extrapolation and visualized isosurfaces at 333 and 500 G in the coronal volume. These dome-like isosurfaces were compared to VLA Stokes V observations, enabling us to estimate an emission height for the polarized emissions and thus the correction required to account for the line-of-sight optical shifting effect. Since the spatial resolution of the F10.7 cm emission is low compared to the EUV, a very small misalignment should not affect the result.

After the alignment between the three instruments has been confirmed, we separate the F10.7 cm contribution into three parts: total intensity (Stokes I; brightness temperature >80,000 K), leading polarized data (positive Stokes V; brightness temperature >10,000 K), and following polarized data (negative Stokes V; brightness temperature <−10,000 K). The spatially averaged FIP bias of these subregions could then be calculated.

2.2. F10.7 cm Radio Flux Observation

Radio observations were made by the JVLA on 2020 April 3 and 7 in the C array configuration (Perley et al. 2011). The observations were made between 14:40 and 21:20 UT on April 3 and between 15:00 and 22:05 UT on April 7 in the 2–4 GHz frequency band. The frequency band was subdivided into 16 subbands, or spectral windows, each with 128 MHz bandwidth. They were each observed with 64 frequency channels of 2 MHz. An integration time of 2 s was used throughout. The high time and frequency resolution enabled radio frequency interference to be identified and excised from a given spectral window. Object 3C 48 was used as the flux and bandpass calibrator, and J0059+006 was used as the gain calibrator on both days. The observations were made in full polarization mode, allowing maps in total intensity (Stokes I) and circularly polarized intensity (Stokes V) to be formed.

Since the field of view of the JVLA is ∼15′, a mosaicking imaging strategy was employed to map the full disk of the Sun; i.e., 19 overlapping fields (Nyquist sampling) were used to provide full disk coverage. For the present work, we focus only on those pointings in which AR 12759 was present and therefore formed maps using only three pointings on each date. Understanding that observations from the JVLA and EIS are not cotemporal, we investigated the temporal evolution of the active region using AIA observations. On April 3, the active region was stable, and on April 7, the active region showed a minor filament activation between its leading and following polarity. This filament has no effect on our analysis. Interferometric instruments such as the JVLA serve as high-pass filters, resolving out emission on large angular scales. For the C array configuration, the background solar disk was effectively resolved out. However, if the total flux from the Sun is known, the background disk can be restored. We did so using a modified version of the feathering technique (Cotton 2015) and the daily observed F10.7 flux densities from the Dominion Radio Astrophysical Observatory.[9]

The resulting maps (shown in Figure 1) provide radio images of AR 12759 with an angular resolution of approximately 9″. These were converted to units of kelvins (brightness temperature) in both Stokes I and V. On April 3, the maximum brightness temperature in the active region in the Stokes I map was $T_B = 2.72 \times 10^5$ K, and on April 7, it was $T_B = 3.74 \times 10^5$ K. The distribution of brightness temperatures on the background disk peaks at $T_B = 3.7 \times 10^4$ K. The Stokes V maps on each day clearly show the bipolar nature of AR 12759. The degree of circular polarization of the active region emission, defined as $\rho_c = V/I$, is low on both days, ranging between −6.6% and +10.2% on April 3 and between −4% and +5.8% on April 7.

2.3. Magnetic Extrapolation and Loop Connectivity

The contribution of thermal gyroresonance emission to F10.7 cm originates in active regions from a thin layer where the emitted frequency (2.8 GHz) is resonant with a low harmonic of the electron gyrofrequency. For coronal conditions, this occurs at the second harmonic layer ($s = 2$) or, more typically, at the third harmonic ($s = 3$) layer (e.g., White & Kundu 1997), corresponding to $B = 500$ and 333 G, respectively. To locate the F10.7 cm gyroresonance emission sites, we modeled the coronal magnetic field of AR 12759 with linear fields extrapolated from photospheric magnetograms using the method of Alissandrakis (1981; Figure 2). This method uses Fourier transforms to find the coronal magnetic field in a volume that satisfies the boundary conditions, including an

[9] https://www.spaceweather.gc.ca/forecast-prevision/solar-solaire/solarflux/sx-4a-en.php

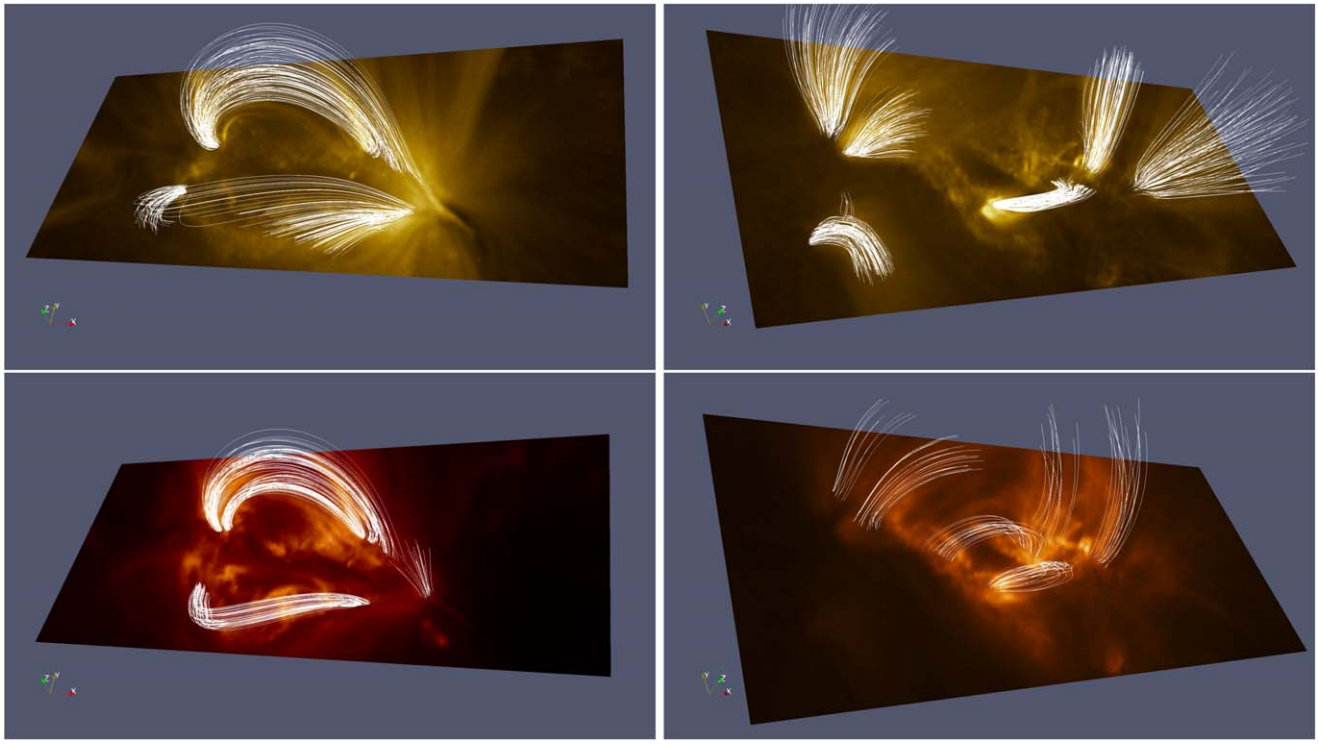

Figure 2. Comparison of extrapolated field lines to AIA observations from the AIA 171 Å (top row) and 193 Å (bottom row) channels on 2020 April 3 (left) and 7 (right). The streamlines show that there is a good match between the magnetic extrapolation used in this paper and the EUV observations.

observed magnetogram at the lower boundary. Many studies have modeled linear force-free magnetic fields using this methodology (e.g., Green et al. 2002; James et al. 2022; Yardley et al. 2022, to name just a few). One limitation of this method is that the maximum value of the force-free parameter, α, that may be used is constrained by the spatial dimensions of the volume (Pevtsov et al. 1995). If α is set too large for the chosen volume, the resulting field will be unphysical, with infinite energy. The boundary magnetograms are taken by the SDO/HMI and are specifically from the Spaceweather HMI Active Region Patch (SHARP) data series (Bobra et al. 2014). This data series provides information about the three-dimensional magnetic field vector in cutouts of the solar surface that contain one active region or more in a cylindrical equal-area (CEA) projection. Each pixel in the CEA projection represents an angular width of $0\overset{\circ}{.}03$, or approximately 0.36 Mm.

We used an iterative method to determine the value of α. We limited the field of view of the magnetogram used in this part of the procedure to include the full extent of the strong magnetic field associated with AR 12759 while excluding as much quiet-Sun noise as possible; furthermore, we only examined pixels where the horizontal field strength is greater than 200 G. We found that the best values of α were $0.06\,\mathrm{CEA}-\mathrm{deg}^{-1}$ on April 3 and $-0.2\,\mathrm{CEA}-\mathrm{deg}^{-1}$ on April 7, which are both less than the maximum α that would still give real solutions in a volume based on the full SHARP magnetogram size. Therefore, we finally modeled the coronal magnetic field of AR 12759 by extrapolating the radial field component of the full HMI SHARP magnetograms taken at 13:36 UT on 2020 April 3 with $\alpha = 0.06\,\mathrm{CEA}-\mathrm{deg}^{-1}$ and 16:00 UT on 2020 April 7 with $\alpha = -0.2\,\mathrm{CEA}-\mathrm{deg}^{-1}$ (Figure 2).

We find a good correspondence between the selected field lines in the extrapolated fields and the coronal loops observed in the EUV channels of SDO/AIA at the same times as the boundary magnetograms used in the extrapolations were taken (examples of 171 and 193 Å are shown in Figure 2), confirming that the linear magnetic fields represent the structure of AR 12759 at the selected times.

The 333 and 500 G isosurfaces in the coronal magnetic field models of the active region on April 3 and 7 are shown in Figure 3. It can be seen that on April 3, the extrapolated isogauss surface of the leading polarity of AR 12759 reaches the greatest height compared to other regions/sets of observations. We conclude that the emission from the lead spot on April 3 is consistent with gyroresonance emission. We placed the JVLA emission maps at different heights in the extrapolation volume to find the height where there was the closest match between the spatial extent of the strong Stokes V emission and the isosurfaces of magnetic field strength. On April 3, there is a good match between the locations of $\pm$10,000 K Stokes V emission and 500 and 333 G radial field strengths. We find that the best spatial match between the Stokes V emission is with the 333 G isogauss surface ($s = 3$) at a height of 2.9 Mm.

3. Results

Figure 1 shows AR 12759 observations obtained on 2020 April 3 and 7. The AIA 193 Å images were used as context, followed by HMI magnetogram, FIP bias, F10.7 cm Stokes V (proxy for gyroresonance), and Stokes I (total intensity) maps. From the AIA 193 Å full disk images shown in Figure 1, we can see that our observations were made when there was minimal solar activity, with AR 12759 the only active region on the disk at the time. Although this active region was small, strong polarized emission can still be observed in the Stokes V map, and the total intensity map traces out the overall morphology of the active region nicely.

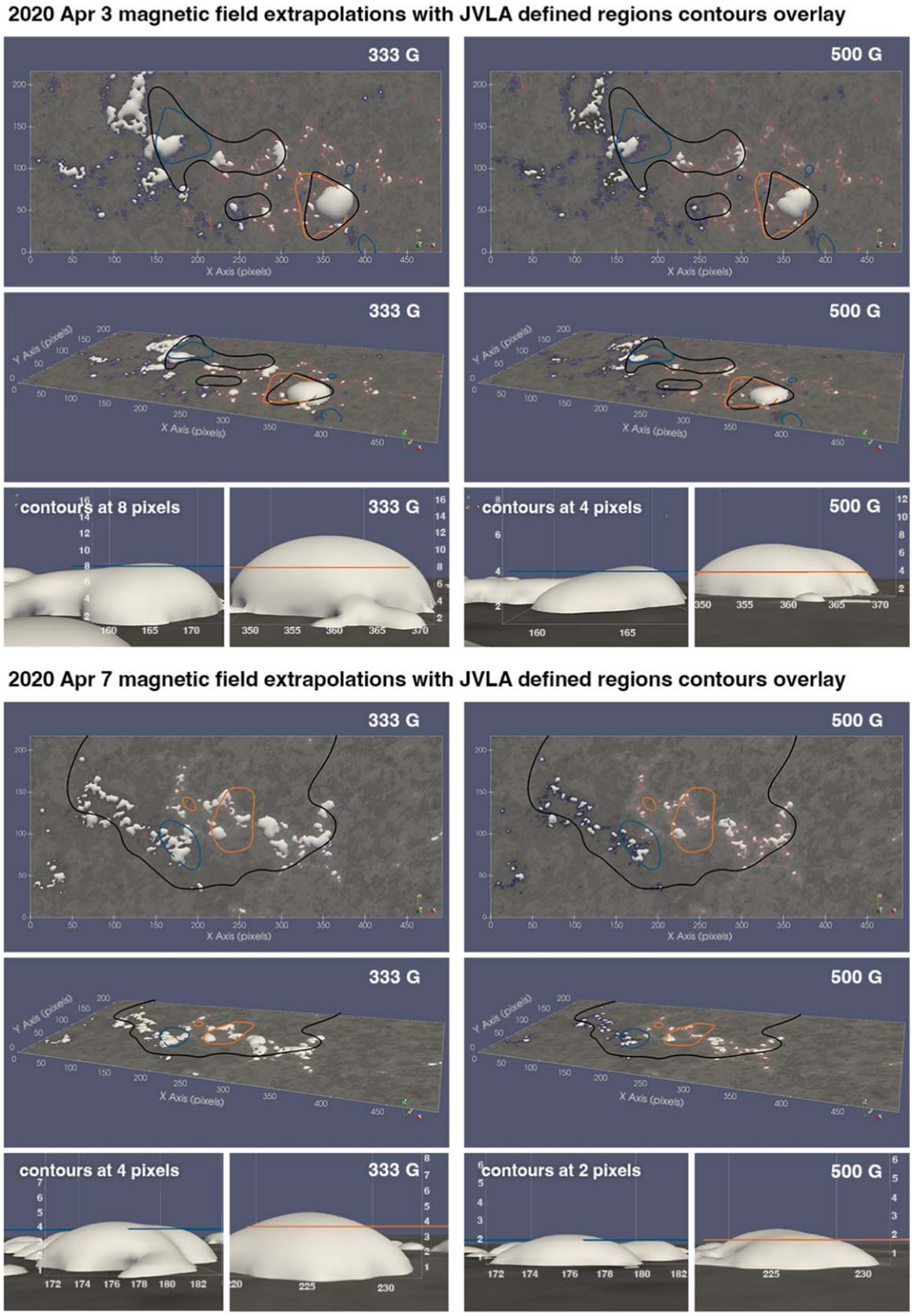

Figure 3. Comparisons between 333 and 500 G isosurfaces (beige domes) in the magnetic field extrapolations to Stokes V emission measured by JVLA on 2020 April 3 (top) and 7 (bottom). Positive and negative radial photospheric magnetic flux are contoured in red and blue, respectively, on the HMI map. Thick black, blue, and orange contours correspond to the regions defined using strong JVLA F10.7 cm emissions in Figure 1, where black is Stokes I > 80,000 K, blue is Stokes V < −10,000 K, and orange is Stokes V >10,000 K. On April 3, the 333 G domes around the JVLA emission reach a height of about 8 pixels (2.90 Mm), and the leading isogauss surface has a much higher height than the following surface, rendering gyroresonance emission. The active region is too weak on April 7 to render emission into gyroresonance.

Table 2
Calculated FIP Bias Values and Magnetic Flux Density Associated with the Two Region-defining Methods

	Contour Regions	FIP Bias	Magnetic Flux Density	Note
Stokes I and Stokes V contours				
2020 Apr 3	Total intensity (Stokes I)	2.7	19.2 G	
	Positive Stokes V	2.6	80.2 G	Leading polarity, orange contour
	Negative Stokes V	3.9	73.7 G	Following polarity, blue contour
2020 Apr 7	Total intensity (Stokes I)	1.6	39.1 G	
	Positive Stokes V	1.7	67.3 G	Leading polarity, orange contour
	Negative Stokes V	1.9	42.1 G	Following polarity, blue contour
Estimated gyroresonance contours ((Stokes I-modeled free–free)/Stokes I)				
2020 Apr 3	Gyroresonance	3.0	44.9 G	Leading polarity, red dashed contour

Note. Top portion of table: regions associated with strong Stokes I and positive and negative Stokes V profiles of the F10.7 cm emission taken on April 3 and 7. Bottom portion of table: region associated with normalized difference (estimated gyroresonance emission region) using ((Stokes I-modeled free–free)/Stokes I) on April 3.

Using JVLA observations, the active region can be dissected into three parts as follows.

1. Leading polarity with strong positive Stokes V emission with brightness temperature >10,000 K.
2. Following polarity with strong negative Stokes V with brightness temperature <−10,000 K.
3. Overall active region indicated by the Stokes I map with a brightness temperature >80,000 K, subtracted by the strong Stokes V regions defined above. This indicates that the region is dominated by free–free (bremsstrahlung) emission.

Three regions were then defined to investigate the relationship between coronal abundances and radio F10.7 flux. These values were chosen to include most of the strongest emitting regions (Figure 1). We then averaged the EIS observed intensities in each of these three regions and calculated the spatially averaged composition value, with the results listed in Table 2. The spatially averaged FIP bias is assumed to have an error of 0.3. Figures 2 and 3 show the magnetic field extrapolation of AR 12759. In Figure 3, white contours indicating strong Stokes V emission are plotted on top of the isogauss surfaces. We see good correlation between Stokes V emission and areas with strong magnetic field strength. Although AR 12759 was small with weak magnetic field strength, distinct differences between the coronal abundances could be observed when the active region was stronger on 2020 April 3. On April 3, over the region with positive Stokes V emission (leading sunspot), the FIP bias is around 2.6. A similar FIP bias value can be observed in the free–free emitting region (FIP bias = 2.7), with the highest FIP bias observed in the negative Stokes V region (FIP bias = 3.9).

However, differences between FIP bias values associated with the three subregions were much smaller or nonexistent on April 7. As shown in the HMI magnetogram in Figure 1, the active region was much weaker on April 7, with no distinct identifiable sunspot. Both of the polarities are much more dispersed on April 7. This seems to have a significant lowering effect on the overall coronal abundance, and the FIP bias remains roughly the same over the three regions, with free–free (FIP bias = 1.6), positive Stokes V (FIP bias = 1.7), and negative Stokes V (FIP bias = 1.9).

4. Discussion

So far, we have analyzed the relationship between FIP bias and Stokes I and V of the F10.7 cm emission. In our first set of observations on April 3, clear differences in FIP bias can be observed between the Stokes I and positive and negative Stokes V regions. Significantly enhanced coronal abundances can be observed associated with the negative Stokes V region (following polarity), whereas we see a much lower FIP bias associated with the positive Stokes V (leading polarity) region. For the second set of observations taken on April 7, this differentiation between subregions completely vanishes. Although we defined contours using the same parameters across the two days, all three regions have roughly the same low FIP bias value of ∼1.7. This inconsistent behavior is extremely interesting, and looking at Figures 1 and 3, the most obvious difference across the two sets of observations is the magnetic field strength or magnetic flux density of each region. From the HMI magnetogram shown in Figure 2, on April 3, the magnetic fields are more closely bound together, whereas by April 7, the magnetic fields are much more dispersed. By comparing the FIP bias to the Stokes I and V profile of the F10.7 radio flux, these results confirm that Stokes V F10.7 cm radio emission comes from the highest magnetic field strength or magnetic flux density areas in the active region. However, not all Stokes V emission may come from gyroresonance emission. In the next section, we try to isolate the gyroresonance regions.

4.1. Region Associated with F10.7 cm Gyroresonance Emission

Since the Stokes V profile contains all of the polarized signal, not only gyroresonance emission, our Stokes V map is inevitably mixed with polarized free–free emission. In order to check if F10.7 cm gyroresonance emission also plays a role in contributing to different FIP biases, we utilize the relationship to relate coronal bremsstrahlung (free–free) emission and DEM,

$$f_\nu = 9.78 \times 10^{-3} \frac{2k_B}{c^2}\left(1 + 4\frac{n_{He}}{n_H}\right) \times \iint T^{-0.5}\ \mathrm{DEM}(T)\mathrm{G}(T)\ dTd\Omega, \quad (1)$$

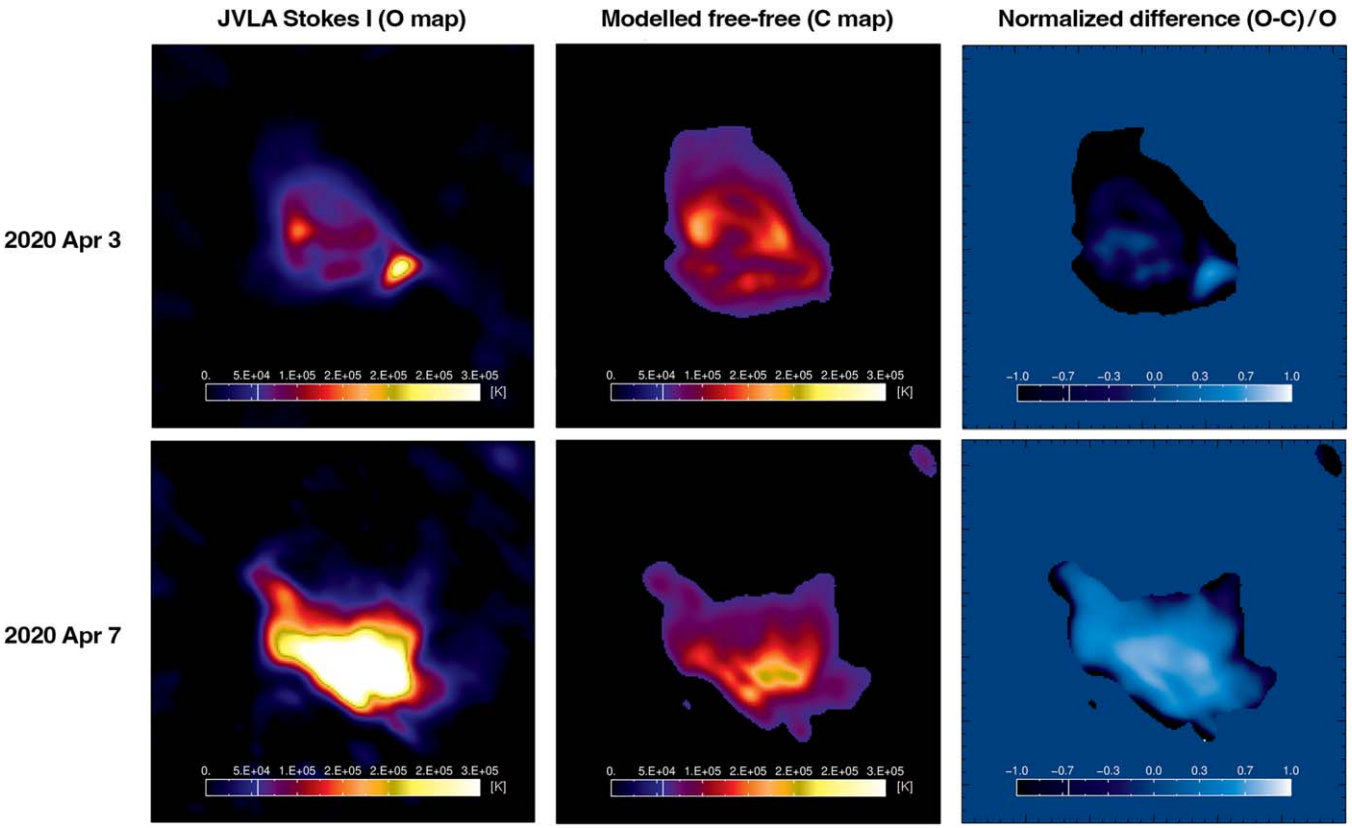

Figure 4. Top to bottom: observations taken by JVLA/EIS on 2020 April 3 and 7. Left to right: JVLA Stokes I observation (O map), modeled F10.7 cm free–free emission calculated using AIA DEM (C map; White et al. 2000 and Schonfeld et al. 2015), and the normalized difference ((O–C)/O map) used to estimate the location of F10.7 cm gyroresonance emission. The modeled free–free map was convolved using an elliptical Gaussian with the dimensions and position angle of the JVLA clean beam to mimic the JVLA observations. On April 3, it can be seen that the estimated gyroresonance region (normalized difference) is associated with the leading sunspot, with the highest magnetic flux density. On April 7, the active region is dispersed and close to the limb, with the possible influence of filament activation. Our analysis is therefore only based on the spot identifiable in the April 3 normalized difference map. Except for the estimated gyroresonance region on April 3, most pixels in the normalized difference maps are within ±0.5, consistent with the results in Schonfeld et al. (2015).

where $k_B = 1.38 \times 10^{-16}\,\mathrm{g\,cm^2\,s^{-2}\,K^{-1}}$ is Boltzmann's constant; $c = 3 \times 10^{10}\,\mathrm{cm\,s^{-1}}$ is the speed of light; $n_{He}/n_H = 0.085$ is the density ratio of helium to hydrogen in the corona; $T(K)$ is the temperature; $G(T) = 24.5 + \ln(T/\nu)$ is the Gaunt factor, where ν is in hertz; and $d\Omega$ is the solid angle of the source (Dulk 1985). Equation (1) shows that the JVLA free–free emission can be estimated using a DEM. Therefore, by calculating the normalize difference ((observed Stokes I—modeled free–free)/observed Stokes I), the remaining signal should indicate the locations of strong gyroresonance emissions.

To model F10.7 cm free–free emission, we used the regularized inversion technique described in Hannah & Kontar (2012) to derive a DEM using the AIA instrument (AIA DEM) for both dates. The derived DEM is then inserted into Equation (1) to generate the modeled free–free map. To achieve results similar to the JVLA observation, we convolved the calculated free–free map using an elliptical Gaussian with the dimensions and position angle of the JVLA clean beam. The results are shown in Figure 4, where we plot the JVLA Stokes I (O map), modeled free–free emission (C map), and normalized difference map (O–C)/O. On April 3, while AR 12759 is still relatively intact, the modeled free–free map shows very good agreement with the JVLA Stokes I map. However, on April 7, the active region has dispersed, and no distinct spot can be identified in the normalized difference map. Also, given that the 333 and 500 G isogauss surfaces are very likely to be within the optically thick layer (Figure 3), gyroresonance emission makes no significant contribution to the observed radio emission. The underestimation of the free–free model could be due to filament activation–related activities on April 7. Except for the regions mentioned above, most pixels in the normalized difference maps are within ±0.5, consistent with the results in Schonfeld et al. (2015).

To investigate the relationship between F10.7 cm gyroresonance emissions and FIP bias, we focus on the April 3 data. As can be seen from the difference map (Figure 4; third column) and the HMI magnetogram (Figure 1; red dashed contour), the observed to predicted maps deviate in the area associated with the leading polarity. As a confirmation, we also used the EIS MCMC DEM technique to model the April 3 spatially averaged free–free emissions at the three regions defined and illustrated in Section 3 and Figure 1, respectively. Using the MCMC DEM calculation method, the modeled free–free emission behaves similarly to the free–free emission calculated by AIA DEM. The blue contour in Figure 1 (following polarity) has the highest modeled free–free emission, followed by the black contour (region between polarities) and finally the orange contour (leading polarity). This is consistent with the AIA DEM method, where a large deviation only exists over the leading polarity. From the magnetic extrapolation, the isogauss surface associated with the leading spot reaches a height of about 8 pixels (2.90 Mm). It is likely that part of this surface is

located at the optically thin region, further suggesting that this is the location of the F10.7 cm gyroresonance source. Therefore, we repeated our composition calculation on this region, and the results are shown in Table 2.

Interestingly, using this second region-defining method using the estimated gyroresonance location, the FIP bias remains roughly the same, maintaining a value of 3.0. These unchanged FIP bias values, yet again, give us a hint of the change in the F10.7–coronal abundance correlation during different levels of solar activity stated in Brooks et al. (2017).

4.2. Interpretation

Overall, we calculated the FIP bias using two different region-defining methods, one taken straight from the JVLA Stokes I and V map and the other using the gyroresonance emission region estimated using DEM calculated with the AIA instrument. From the first method, the leading region has a slightly enhanced FIP bias value of 2.6, whereas the following region shows significantly enhanced coronal abundances at FIP bias = 3.9. As we move on to the second region-defining method, using a region associated with gyroresonance emission, the leading spot shows a FIP bias of around 3.0, a value that is still a lot lower than the FIP bias found in the more dispersed negative Stokes V area. We believe that the combination of these two methods tells the same story: magnetic field strength plays a crucial role in the variation of coronal abundances. On April 3, the active region still contains sunspots, and the overall FIP bias value is higher when compared to observations taken on April 7. However, as we zoom into the small subregions, different magnetic concentrations contribute differently to the FIP bias observed. In both of the region-defining methods, the leading polarity has always been associated with a stronger, more concentrated magnetic field. Under this configuration, the magnetic fields associated with this emission inhibit convection. The consequent cooler temperatures lead to a lower ionization rate and thus a slightly lower FIP bias (Baker et al. 2021; Mihailescu et al. 2022). In contrast, in the following spot, roughly the same magnetic flux is spread out into a larger area. The higher temperatures lead to a higher ionization rate of the low-FIP elements. Our result shows similar behavior to the sunspots investigated in Mihailescu et al. (2022), who also found a slightly lower FIP bias value in the leading polarity sunspot region with higher magnetic flux density.

This result can be translated into a bigger picture, informing us on the relationship between Sun-as-a-star FIP bias and F10.7 flux. According to the ponderomotive force model of fractionation developed by Laming (2015), nanoflares caused by the reconnection of a braided magnetic field in the corona trigger Alfvén waves that travel down to the field line's footpoint in the chromosphere. These Alfvén waves are being repeatedly refracted and reflected in the strong density gradient of the chromosphere, initiating the ponderomotive force, which brings ions to the corona, contributing to what we quantify as FIP bias (Laming 2015, 2021). In this context, when the solar activity is low, overall coronal abundances behave similarly to AR 12759 on April 7. Magnetic flux is low in the activity belt, and the lower nanoflare activity and consequently lower resonant Alfvén wave activity in the coronal loops result in a lower Sun-as-a-star FIP bias during solar minimum. Then, as solar activity ramps up, more regions of strong fields and nanoflares contribute to more Alfvén waves being created and reflected along closed magnetic loops. The FIP bias slowly goes up with the solar activity. As F10.7 cm radio flux is a proxy for solar activity, we expect Sun-as-a-star FIP bias to correlate extremely well with F10.7 cm measurements under the above scenarios. However, during peak solar activity, more and more gyroresonance emissions start to mix into the F10.7 index. As a whole, although we have higher F10.7 flux, the FIP bias values stop changing, resulting in the change in correlation we see in Brooks et al. (2017).

5. Conclusions

In this paper, we present observations of a small active region, AR 12759, using Hinode/EIS, JVLA, and SDO/AIA. This active region was in its decay phase, initially containing a leading sunspot and trailing pores before decaying to only dispersed magnetic flux with no spots on 2020 April 7. There are significant differences between the magnetic field strengths (flux densities) observed on 2020 April 3 and 7. We employed two region-defining methods to investigate the relationship between the FIP bias and the different emission mechanisms of the F10.7 radio flux, one defined using the Stokes I and V maps and the other using the estimated gyroresonance region isolated with the help of both the Stokes I map and AIA DEM. Combining the results from the two methods, we find that the following polarity region carries a significantly enhanced Si/S coronal abundance. In contrast, in the leading polarity, no matter how we alter the region-defining method, the FIP bias enhancement seems to be weaker, maintaining a value slightly higher than the quiet Sun.

This analysis is consistent with the findings in Brooks et al. (2017). Under low–medium solar activity (or, in other words, when there is no/low gyroresonance emission), magnetic flux density plays an important role in varying elemental fractionation. At the start of the solar cycle, active regions (their sunspots) are smaller than the ones that emerge later in the cycle (Watson et al. 2011; Valio et al. 2020). The Sun-as-a-star FIP bias rises with the appearance of each new active region and the increased heating rate within. As each active region evolves, its decay (dispersion to a plage-like magnetic flux density) further increases the overall FIP bias, as we found when comparing the spot-containing leading and plage-like following polarity areas in AR 12759 on April 3. At the end, as we found on April 7, during the late decay phase of an active region, the FIP bias decreases. Under such low-activity, low-gyroresonance conditions, the FIP bias and F10.7 cm emission show a good correlation.

However, as activity rises toward the solar maximum, the maximum sunspot area increases, and spots have higher field strength and become cooler (Watson et al. 2011; Valio et al. 2020). This was, in particular, confirmed as being the case for the 2009–2014 period by Rezaei et al. (2015). We suggest that under high solar activity conditions with rising sunspot area and field strength, the contribution of gyroresonance emission to the F10.7 cm emission will likely increase. As with the second method, we found that while coronal abundances maintain roughly the same level in regions of high magnetic flux density, the gyroresonance radio flux from these spotted areas is not lower but rather significantly higher than that from plage regions. So we postulate that the distinctly different tendencies of radio gyroresonance emission and coronal abundances (FIP bias) over strong magnetic field concentrations (sunspots) are the likely cause of the saturation of Sun-as-

a-star coronal abundances around solar maximum. Amid this FIP bias saturation, the F10.7 index, with its combined contribution from both free–free (bremsstrahlung) and gyroresonance components, remains well correlated with the sunspot number and other magnetic field proxies, creating this nonlinear correlation in Brooks et al. (2017).

Our observations provide a glimpse into the reason behind the nonlinear relationship during solar maximum. However, the fact that our JVLA–EIS joint observations were made during solar minimum on a small active region relatively close to the solar limb has limited our ability to further investigate the relationship between magnetic field behavior and FIP bias. Taking several observations of different active regions when the Sun is more active would be important to confirm our finding. Ideally, a statistical sample of EIS and JVLA maps could be built up from solar minimum to solar maximum to fully understand the correlation and scaling between F10.7 flux and coronal abundances. Also, although we have gone to great lengths to minimize the effects that arise from differences in the line of sight, observations of Sun-centered active regions could further reduce the alignment uncertainty. Since F10.7 radio flux comes from a wide range of solar altitudes, adding observations using the Solar Orbiter, in particular, Spectral Imaging of the Coronal Environment (SPICE), can add another layer of analysis and further constrain our results from the corona to the chromosphere. The upcoming Solar-C EUV High-throughput Spectroscopic Telescope (EUVST) and its wide range of cotemporal temperature coverage can also contribute massively by observing different layers of the Sun's atmosphere simultaneously. It is worth noting that in this paper, we have focused on observations of one active region. It is important not to dismiss that during solar maximum, we have many more on disk coronal holes and intense flares. These coronal holes and flares also play a role in lowering the Sun-as-a-star FIP bias during solar maximum. Although our finding shows great consistency with previous studies, more observations on coronal holes/flares are required to precisely disentangle the relationship between F10.7 cm and Sun-as-a-star FIP bias.

Apart from solar composition, our result could be extended to the context of stellar coronal composition. Low-activity stars like our Sun have coronae that are dominated by the FIP effect (a more enhanced low-FIP composition). This result highlights the importance of magnetic field strength or magnetic flux density and the F10.7 cm emission when linking coronal composition to the different spectral types of stars. In addition to the stellar coronal composition investigation done in Wood & Linsky (2010) and Seli et al. (2022), a full-cycle observation should also be considered to fully understand stellar composition variability.

We thank the reviewer for the very constructive comments. A.S.H.T. thanks the STFC for support via funding given in his PhD studentship. A.W.J. is supported by a European Space Agency (ESA) Research Fellowship. D.M.L. is grateful to the Science Technology and Facilities Council for the award of an Ernest Rutherford Fellowship (ST/R003246/1). The work of D.H.B. was performed under contract to the Naval Research Laboratory and funded by the NASA Hinode program. D.B. is funded under STFC consolidated grant No. ST/S000240/1, and L.v.D.G. is partially funded under the same grant. L.v.D.G. acknowledges Hungarian National Research, Development and Innovation Office grant OTKA K-113117. G.V. acknowledges the support from the European Union's Horizon 2020 research and innovation program under grant agreement No. 824135 and from STFC grant No. ST/T000317/1. Hinode is a Japanese mission developed and launched by ISAS/JAXA, with NAOJ as domestic partner and NASA and STFC (UK) as international partners. It is operated by these agencies in cooperation with ESA and NSC (Norway). The AIA data are courtesy of NASA/SDO and the AIA, EVE, and HMI science teams. CHIANTI is a collaborative project involving George Mason University, the University of Michigan (USA), and the University of Cambridge (UK). The National Radio Astronomy Observatory is a facility of the National Science Foundation operated under cooperative agreement by Associated Universities, Inc. A.S.H.T. thanks Dr. Hamish Reid for a fruitful discussion after the FASR 2021 conference.

Appendix

In this section, we show the AIA DEM used to model the F10.7 cm free–free emission on 2020 April 3. The DEM in Figure 5 shows that the core loops of the active region have a temperature of $\log T = 6.0$–6.1.

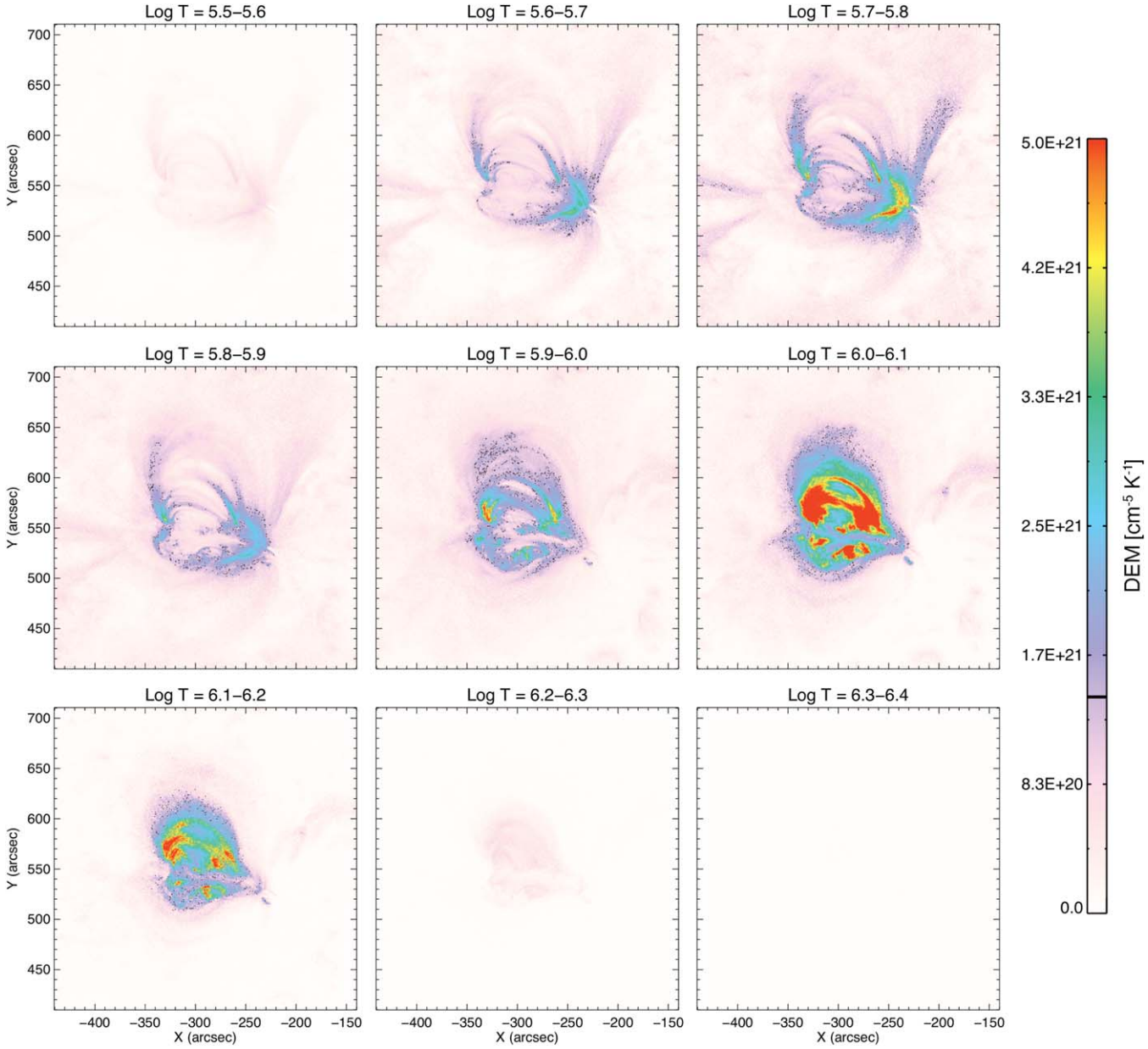

Figure 5. The DEM on April 3 calculated using AIA passbands (Hannah & Kontar 2012). The DEM shows that the simple active region has a relatively low temperature, with a majority of emission from log $T = 6.0$–6.1.

ORCID iDs

Andy S. H. To https://orcid.org/0000-0003-0774-9084
Alexander W. James https://orcid.org/0000-0001-7927-9291
T. S. Bastian https://orcid.org/0000-0002-0713-0604
Lidia van Driel-Gesztelyi https://orcid.org/0000-0002-2943-5978
David M. Long https://orcid.org/0000-0003-3137-0277
Deborah Baker https://orcid.org/0000-0002-0665-2355
David H. Brooks https://orcid.org/0000-0002-2189-9313
Samantha Lomuscio https://orcid.org/0000-0002-0027-0372
David Stansby https://orcid.org/0000-0002-1365-1908
Gherardo Valori https://orcid.org/0000-0001-7809-0067

References

Alissandrakis, C. E. 1981, A&A, 100, 197
Baker, D., Brooks, D. H., Démoulin, P., et al. 2013, ApJ, 778, 69
Baker, D., Brooks, D. H., Démoulin, P., et al. 2015, ApJ, 802, 104
Baker, D., Brooks, D. H., van Driel-Gesztelyi, L., et al. 2018, ApJ, 856, 71
Baker, D., Stangalini, M., Valori, G., et al. 2021, ApJ, 907, 16
Bobra, M. G., Sun, X., Hoeksema, J. T., et al. 2014, SoPh, 289, 3549
Brooks, D. H., Baker, D., van Driel-Gesztelyi, L., & Warren, H. P. 2017, NatCo, 8, 1
Brooks, D. H., & Warren, H. P. 2011, ApJL, 727, L13
de Wit, T. D., Bruinsma, S., & Shibasaki, K. 2014, JSWSC, 4, A06
Del Zanna, G., & Mason, H. E. 2014, A&A, 565, A14
Dere, K. P., Del Zanna, G., Young, P. R., Landi, E., & Sutherland, R. S. 2019, ApJS, 241, 22
Dere, K. P., Landi, E., Mason, H. E., Fossi, B. C. M., & Young, P. R. 1997, A&AS, 125, 149

Dulk, G. A. 1985, ARA&A, 23, 169
Feldman, U., Schühle, U., Widing, K. G., & Laming, J. M. 1998, ApJ, 505, 999
Felli, M., Lang, K. R., & Willson, R. F. 1981, ApJ, 247, 325
Floyd, L., Newmark, J., Cook, J., Herring, L., & McMullin, D. 2005, JASTP, 67, 3
Green, L. M., López fuentes, M. C., Mandrini, C. H., et al. 2002, SoPh, 208, 43
Grevesse, N., Asplund, M., & Sauval, A. J. 2007, SSRv, 130, 105
Hannah, I. G., & Kontar, E. P. 2012, A&A, 539, A146
Henney, C. J., Toussaint, W. A., White, S. M., & Arge, C. N. 2012, SpWea, 10, S02011
James, A. W., Williams, D. R., & O'Kane, J. 2022, A&A, 665, A37
Kashyap, V., & Drake, J. J. 1998, ApJ, 503, 450
Kashyap, V., & Drake, J. J. 2000, BASI, 28, 475
Kasper, J. C., Stevens, M. L., Lazarus, A. J., Steinberg, J. T., & Ogilvie, K. W. 2007, ApJ, 660, 901
Ko, Y.-K., Young, P. R., Muglach, K., Warren, H. P., & Ugarte-Urra, I. 2016, ApJ, 826, 126
Laming, J. M. 2015, LRSP, 12, 2
Laming, J. M. 2021, ApJ, 909, 17
Lemen, J. R., Title, A. M., Akin, D. J., et al. 2012, SoPh, 275, 17
Lepri, S. T., Landi, E., & Zurbuchen, T. H. 2013, ApJ, 768, 94
McIntosh, S. W., Kiefer, K. K., Leamon, R. J., Kasper, J. C., & Stevens, M. L. 2011, ApJL, 740, L23
Mihailescu, T., Baker, D., Green, L. M., et al. 2022, ApJ, 933, 245
Perley, R. A., Chandler, C. J., Butler, B. J., & Wrobel, J. M. 2011, ApJL, 739, L1
Pesnell, W. D., Thompson, B. J., & Chamberlin, P. C. 2012, SoPh, 275, 3
Pevtsov, A. A., Canfield, R. C., & Metcalf, T. R. 1995, ApJL, 440, L109
Rezaei, R., Beck, C., Lagg, A., et al. 2015, A&A, 578, A43
Scherrer, P. H., Schou, J., Bush, R. I., et al. 2012, SoPh, 275, 207
Schmahl, E. J., & Kundu, M. R. 1995, JGR, 100, 19851
Schmahl, E. J., & Kundu, M. R. 1998, in ASP Conf. Ser. 140, Synoptic Solar Physics, ed. K. S. Balasubramaniam, J. Harvey, & D. Rabin (San Francisco, CA: ASP), 387
Schonfeld, S. J., White, S. M., Henney, C. J., Arge, C. N., & McAteer, R. T. J. 2015, ApJ, 808, 29
Schonfeld, S. J., White, S. M., Henney, C. J., Hock-Mysliwiec, R. A., & McAteer, R. T. J. 2019, ApJ, 884, 141
Schonfeld, S. J., White, S. M., Hock-Mysliwiec, R. A., & McAteer, R. T. J. 2017, ApJ, 844, 163
Seli, B., Oláh, K., Kriskovics, L., et al. 2022, A&A, 659, A3
Tapping, K. F. 2013, SpWea, 11, 394
Tapping, K. F., Cameron, H. T., & Willis, A. G. 2003, SoPh, 215, 357
Tapping, K. F., & Detracey, B. 1990, SoPh, 127, 321
To, A. S. H., Long, D. M., Baker, D., et al. 2021, ApJ, 911, 86
Valio, A., Spagiari, E., Marengoni, M., & Selhorst, C. L. 2020, SoPh, 295, 120
Warren, H. P. 1999, SoPh, 190, 363
Watson, F. T., Fletcher, L., & Marshall, S. 2011, A&A, 533, A14
White, S. M., & Kundu, M. R. 1997, SoPh, 174, 31
White, S. M., Thomas, R. J., Brosius, J. W., & Kundu, M. R. 2000, ApJL, 534, L203
Wood, B. E., & Linsky, J. L. 2010, ApJ, 717, 1279
Woods, T. N., Eparvier, F. G., Hock, R., et al. 2012, SoPh, 275, 115
Yardley, S. L., Green, L. M., James, A. W., Stansby, D., & Mihailescu, T. 2022, ApJ, 937, 57